Geometry and magnetism of L1$_0$ nanostructures

Kory D. Sorge
University of Nebraska-Lincoln, sorge@physics.fau.edu

Ralph Skomski
University of Nebraska-Lincoln, rskomski2@unl.edu

Maria Daniil
University of Nebraska - Lincoln, mdaniil2@unl.edu

Steven A. Michalski
University of Nebraska-Lincoln, smichalski2@unl.edu

L. Gao
University of Nebraska - Lincoln

See next page for additional authors

Authors

Kory D. Sorge, Ralph Skomski, Maria Daniil, Steven A. Michalski, L. Gao, Jian Zhou, M. Yan, Yucheng Sui, Roger D. Kirby, Sy_Hwang Liou, and David J. Sellmyer

Geometry and magnetism of L1$_0$ nanostructures

K.D. Sorge, R. Skomski, M. Daniil, S. Michalski, L. Gao, J. Zhou,
M. Yan, Y. Sui, R.D. Kirby, S.H. Liou and D.J. Sellmyer

Department of Physics and Astronomy and Center for Materials Research and Analysis
University of Nebraska–Lincoln
Lincoln, NE 68588, USA

Abstract

The fabrication and magnetism of L1$_0$ nanostructures with different shapes (such as nanoparticles and nanotubes) is investigated. These nanostructures are produced by hydrogen processing and focused ion beam milling. The structures exhibit interesting reversal modes and are of present or potential interest for sensors and imaging, as well as magnetic recording.

Keywords: High coercivity materials; Magnetic reversal; Magnetic nanostructures; Nanostructure fabrication

1. Introduction

Thin-film nanostructures, such as dots, antidots, rings, and wires, are scientifically interesting model systems with many present and future technological applications. There has been considerable work on soft-magnetic systems, such as Fe, Ni, and permalloy, but magnets with well-defined magnetocrystalline anisotropies, such as L10 nanostructures, are a relatively recent trend. Compared to bulk L10 magnets, whose nanostructure reflects the involved metallurgy of the system [1], thin-film nanostructuring offers far-reaching specific opportunities to artificially control and tune the performance of the magnets. Examples are highly coercive nanodots [2] and [3] and particulate L10 magnets [4] and [5] for magnetic recording applications.

There are many ways to fabricate these magnetic nanostructures, including both bulk and thin-film techniques. Thin-film methods range from sputtering and molecular-beam epitaxy [2] and [6] to cluster deposition [7] and [8], laser-interference lithography [9], hydrogen processing [10] and [11], organic chemical synthesis [12] and [13], and focused ion beam milling (FIB) [14], [15] and [16]. Most methods applicable to other nanoscale systems can be used to produce L10 magnets.

Here we explore L10 magnets in novel nanoscale geometries. Two techniques for making these structures that we focus on are FIB milling of larger structures and films as well as templated growth by hydrogen reduction. The unique geometries presented offer insight as to how even fundamental behavior of these systems (such as the reversal mode) depend on the shape, in addition to the size, at the nanoscale.

2. L10 tips for magnetic force microscopy

The control of the geometry of hard-magnetic tips for magnetic force microscopy (MFM) is a condition for the investigation of high-density recording media. Widely available microscopes and magnetic tips yield images with resolutions down to 50 nm, but further improvements have remained a challenge. One strategy is to exploit the high magnetocrystalline anisotropy and coercivity of CoPt. The idea is to use FIB milling to improve the MFM resolution by producing dipolar tip ends that exhibit a stable magnetization and are well separated from other nanoscale magnetic field sources, except for the film to be investigated.

First, a 30 nm CoPt film is deposited on commercially available MFM cantilevers and annealed at 650 °C for 10 h to order the CoPt into the L10 crystal structure. FIB is then used to remove the magnetic material around the apex, leaving a 30 nm diameter magnetic particle at the tip end. Due to the smaller amount of magnetic material, the stray field from this new tip is significantly reduced, and the spatial resolution of the magnetic domain images is improved. In addition, the probe tip has a much smaller likelihood of switching from stray fields being measured because of the magnetically hard CoPt particle. The tip can been used to obtain images with a spatial resolution between 11 and 28 nm [17].

Fig. 1 shows an electron micrograph of a typical CoPt tip. The tip was first coated by CoPt and then modified by FIB milling with a Ga beam energy of 30 keV and a beam current of 4 pA. Because the Ga ions degrade the magnetic properties of the magnetic material, exposure to the ions should be minimized to avoid damage [18] and [19]. For this, the tip is milled from the side, that is, the ion beam direction is perpendicular to the tip axis.

3. Magnetic nanotubes

Hydrogen reduction processing is a highly efficient approach to template-directed chemical synthesis. In practice, it is very similar to nanoparticle fabrication by organic chemistry and has recently [10] been used to produce both FePt and Fe3O4 nanotubes in nanochannels of porous alumina templates.

The template alumina substrates are purchased commercially and have a nominal pore size of 200 nm. For consistent results, all templates are pre-annealed in air at 600 °C for 10 min to oxidize all aluminum and remove water from the pores.
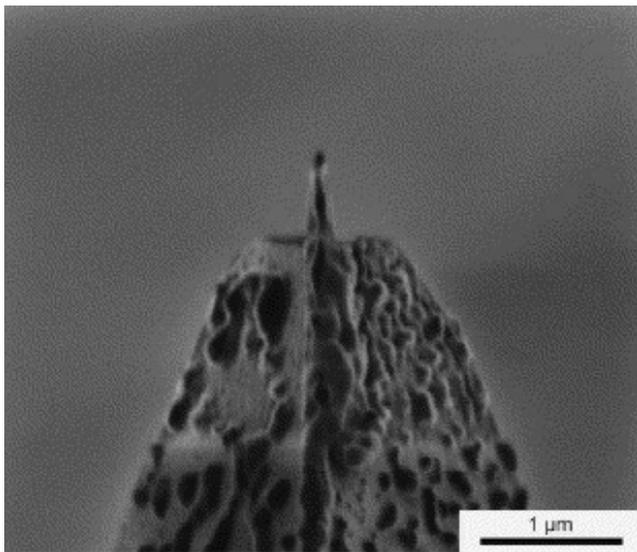
Fig. 1. FIB milled MFM tip shows a magnetic particle with a diameter of 80 nm at the tip end.

To produce the L10 nanotubes, the substrates are wetted with alcohol and loaded with a mixture of H2PtCl6 • 6H2O and FeCl3 • 6H2O having an Fe:Pt atomic ratio of 1:1. The loaded templates are then mounted on a sample holder, with pores horizontal, and placed in an oven with flowing hydrogen for 1.5 h at 560 °C. After the nanotubes have formed, samples are etched in an 0.3 M NaOH aqueous solution and the precipitates dispersed in acetone.

Fig. 2a shows a transmission electron microscope image of the FePt sample taken after etching for 50 min and being dispersed in acetone. The image is, actually, a composite tube of FePt encased by alumina. This alumina case is retained to insure that the fragile tube remains intact. Considering the laminar growth of Co on an Al2O3 substrate [20], it is reasonable to assume a chemical bond between the interface of the FePt alloy and the inner walls of the nanochannels. The length of these nanotubes is about 0.5 mm and their diameters range from about 150 to 220 nm, depending on the thickness of the template film and the pore diameter distribution. XRD data reveal that the FePt crystallizes in the tetragonal L10 structure. This is consistent with measured coercivity in the range of 2.09 T, shown in **Fig. 2**b.

4. Magnetic nanorings

Magnetic nanorings can be formed by FIB milling on films with pre-formed magnetic texture. This geometry is particularly nice when dealing with $L1_0$ magnets because of access to the easier curling reversal mode. A specific theoretical prediction is that reversal by curling is much more favorable than the reversal by coherent rotation. It can be shown that the main reason is the absence of vortex singularities in the center of the structures.

FePt:Ag nanorings are produced by magnetron sputtering and focused ion beam (FIB) milling. First, highly anisotropic $L1_0$-phase FePt(0 0 1) films are prepared by sputtering a multilayer of $[Ag(1Å)/\{Fe(3.81 Å)/Pt(4 Å)\}_2]_8$ on oxidized Si{0 0 1} wafers and then rapid thermal annealing at 600 °C. After annealing, grains of FePt embedded in Ag are formed. A protective layer of Al is then deposited to protect
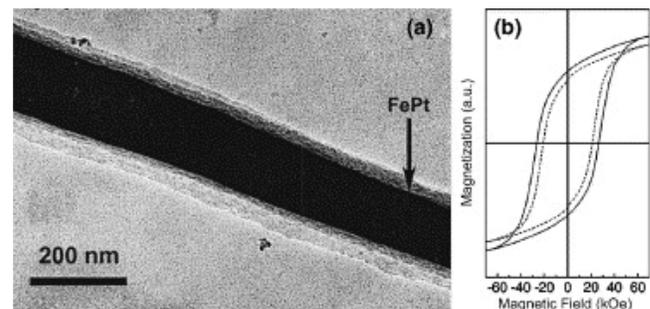
Fig. 2. (a) FePt nanotube produced by hydrogen processing and encased in alumina. (b) Magnetic measurements show that the FePt is in the $L1_0$ phase. The solid curve is data taken at 5 K, while the dashed curve was measured at room temperature.
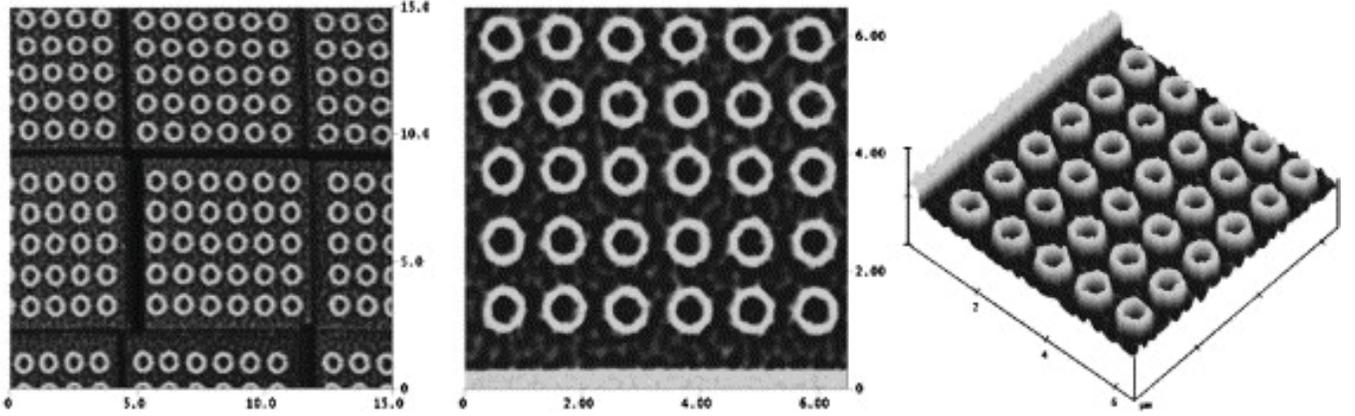
Fig. 3. Arrays of magnetic nanorings formed by focused ion beam milling on FePtAg multilayers.

the film during patterning, but later removed by chemical etching. After patterning, the resulting structures are studied by atomic force microscopy (AFM), MFM, and magneto-optic Kerr effect (MOKE).

Rings with outer ring diameter $d = 750$ nm, width $w = 135$ nm, and edge-to-edge separation $s = 300$ nm are illustrated in the AFM image in Fig. 3. Using this technique, it is possible to pattern a film area of 30×30 μm^2 at one time.

Kerr hysteresis loops shows significant perpendicular coercivity ($H_c = 89$ mT). The loops, however, are far from being rectangular because milling somewhat deteriorates the quality of the film. This is illustrated in Fig. 4, where MOKE hysteresis loops from an unpatterned and patterned region are shown. One strategy to increase the ring crystallinity and improve the loop shape might be a subsequent annealing step following milling. By this, the implanted Ga ions will have a chance to diffuse out of the rings and the FePt can recrystallize.

The method makes it possible to realize virtually any geometry, with some restrictions applying to features smaller than 100 nm. However, the FIB milling destroys the nearly perfect c-axis alignment of the starting films, and the structures are probably best described as partially aligned (textured) with some atomic disorder.

5. Magnetization modes

For magnetic recording and other applications, it is necessary to understand both the remanent magnetization states and the magnetization configurations (or modes) during magnetization reversal. Fig. 5 summarizes these spin structures for idealized structures corresponding to Sections Sections 2, 3, and 4. The magnetization modes $\mathbf{M(r)}$ can be written as $\mathbf{M} = M_s(\sqrt{1-m^2}\mathbf{e}_z + \mathbf{m})$, where $\mathbf{m} = \mathbf{m}_x\mathbf{e}_x + \mathbf{m}_y\mathbf{e}_y$ is a perpendicular magnetization component. In the absence of magnetostatic interactions and imperfections, the mode $\mathbf{m}$ obeys [14]

$$A\nabla^2\mathbf{m} + (K_1 + \mu_0 M_s H/2)\mathbf{m} = 0. \qquad (1)$$

Fig. 4. MOKE hysteresis loops of FePt:Ag films in an unpatterned and patterned region.
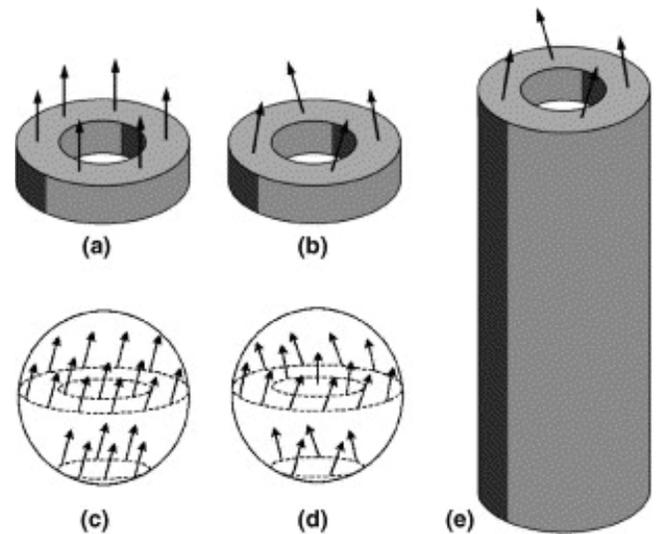
Fig. 5. Magnetization states in magnetic nanostructures: (a) coherent remanent state in nanorings, (b) curling in nanorings, (c) coherent rotation in spherical nanoparticles, (d) curling in spherical nanoparticles, and (e) curling in nanotubes.

The magnetization modes $\mathbf{m}(x,y,z)=\mathbf{m}(\rho,\phi,z)$ are obtained as eigenmodes of **Eq. (1)** subject to 'free' boundary conditions $\mathbf{n}_s \cdot \nabla \mathbf{m}=0$ at the surface, where $\vec{\mathbf{n}}_s$ is the surface normal. For cylindrical symmetries, the solution of the problem involves Bessel functions.

In nanowires, $\mathbf{m}(\rho,\phi,z)=m_{xy}(\rho,\phi)m_z(z)\mathbf{e}_m$, where $m_{xy}(\rho,\phi)$ is a relatively complicated function [14]. In nanotubes, the situation is even more involved, particularly since magnetostatic flux closure can no longer be ignored. For example, the transition between coherent rotation and curling occurs at a tube diameter of the order of 5 nm, as opposed to about 20 nm for nanowires. The reason is the absence of a 'core' at $\rho = 0$, that is, the absence of the energetically unfavorable requirement that $\mathbf{M}=M_s\mathbf{e}_z$ at $x = y = 0$, as in the case of the central spin in **Fig. 5d.** In terms of **Eq. (1)**, these contributions amount to the addition of terms that mix m_x and m_y.

An essential simplification is encountered when the tube thickness $R_{max} - R_{min}$ is much smaller than the tube diameter $2R_{max}$. Then the low-lying modes have the character of 'plane' waves subjected to the quantization condition $\mathbf{m}(\rho, \phi+2\pi,z)=\mathbf{m}(\rho,\phi,z)$. **Fig. 6** shows the corresponding magnon densities of states and the real-space character of the corresponding modes $m_{xy}(\rho,\phi)$. The finite peak width is caused by spin waves that travel parallel to the tube axis, $\mathbf{m}\sim\exp(ik_z z)$. Note that the low-lying states shown in **Fig. 6** are all magnetostatically favorable, because there are no magnetization components perpendicular to the surface. The magnetostatic self-energies of the modes having a magnetization component perpendicular to the surface are larger by a factor of order $(R_{max} - R_{min})/R_{max}$. They, as well as the highly energetic radial contributions, can therefore be ignored in lowest order.
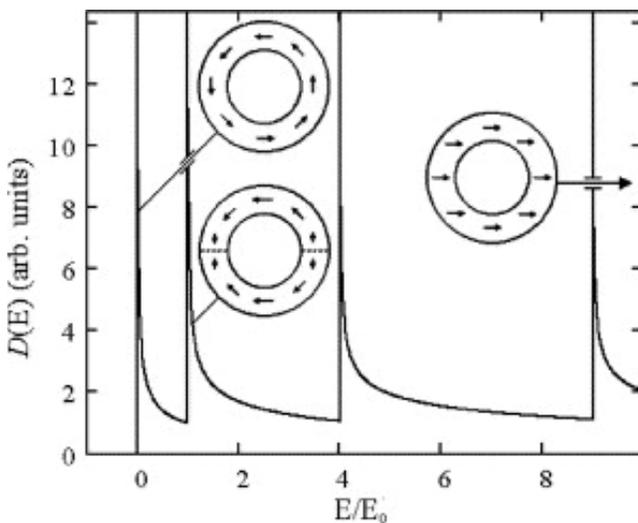
6. Discussion and conclusions

The modes shown in **Fig. 5** are idealized, because they ignore effects such as polycrystallinity and incomplete L1$_0$ ordering. **Fig. 7** illustrates the difference between ideal and real nanotube systems discussed in Section 3. A consequence of the polycrystalline nature of the nanotubes, shown in **Fig. 7**c, is a localization of the nucleation modes along the tube axis, very similar to the previously discussed [21] case of nanowires.

In nanorings, there are two types of effects. First, in ideal rings, the finite height leads to a strong magnetization-mode (or spin-wave) quantization parallel to the z-axis. As a consequence, the component $\mathbf{m} \sim \exp(ik_z z)$ is no longer quasi-continuous, and the peaks in **Fig. 6** must be replaced by sets of well-separated sharp levels. Second, the ion-beam milling is likely to yield some disorder, thereby broadening the peaks. Coercivity is an extremely susceptible, though difficult to quantify, indicator of mode-distortions due to structural imperfections and chemical disorder [22]. In the present case, the relatively low coercivity, about 89 mT, indicates a significant degree of disorder.

In conclusion, it is possible to produce a wide range of L1$_0$ nanostructures with varying geometries and intriguing magnetic properties. Our focus has been on nanorings and nanotubes formed by ion beam milling and templated hydrogen processing. In hydrogen processing, L1$_0$ ordered FePt tubes are formed in a template porous alumina matrix. The length of these tubes is about 0.5 mm and diameters range from 150 to 220 nm. FIB milling can be used to make nanorings of partially textured FePt. Rings with a wall width of 135 nm and outer diameter of 750 nm show a significant perpendicular coercivity, although loop shape is far from rectangular. These new geometries alter not only the reversal mode at nanoscale dimensions, but also the nature of the excited modes.

Fig. 6. Magnon densities of states $D(E)$ for ideal nanotubes with $R_{max} - R_{min} \ll R_{max}$. The spacing of the peaks decreases with increasing tube diameter D, $E_0 \sim A/D^2$, and depends on the magnetization. Within the limits considered, the coherent state has a relatively high energy.
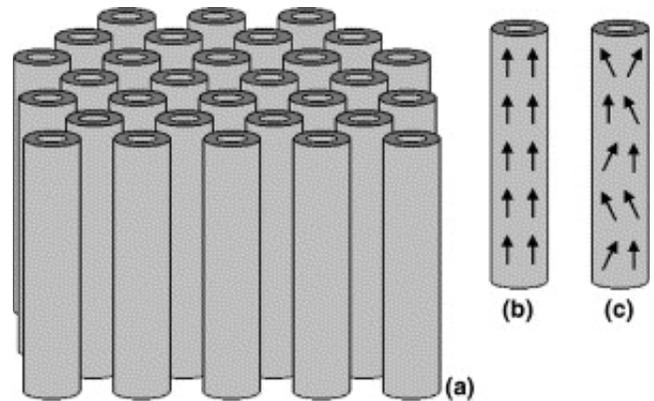
Fig. 7. Ideal and imperfect nanotubes: (a) nanotube array, as embedded in porous Al$_2$O$_3$, (b) remanent magnetization state in perfect nanotubes, and (c) remanent magnetization state in imperfect nanotubes. By geometry, the outer tube radius R_{max} is equal to the alumina pore radius.

References

[1] T. Klemmer, D. Hoydick, H. Okumura, B. Zhang and W.A. Soffa, *Scr Metall Mater* **33** (1995), p. 1793.

[2] T. Shima, K. Takanashi and K. Hono, *Appl Phys Lett* **81** (2002), p. 1050.

[3] T. Shima, K. Takanashi, Y.K. Takahashi and K. Hono, *Appl Phys Lett* **85** (2004), p. 2571.

[4] Y. Shao, M.L. Yan and D.J. Sellmyer, *J Appl Phys* **93** (2003), p. 8152.

[5] M.L. Yan, R. Skomski, A. Kashyap, L. Gao and S.H. Liou *et al.*, *IEEE Trans Magn* **40** (2004), p. 2495.

[6] J.U. Thiele, L. Folks, M.F. Toney and D.K. Weller, *J Appl Phys* **84** (1998), p. 5686.

[7] D.L. Peng, T. Hihara and K. Sumiyama, *Appl Phys Lett* **83** (2003), p. 350.

[8] J.M. Meldrim, Y. Qiang, Y. Liu, H. Haberland and D.J. Sellmyer, *J Appl Phys* **87** (2000), p. 7013.

[9] M. Zheng, M. Yu, Y. Liu, R. Skomski and S.H. Liou *et al.*, *Appl Phys Lett* **79** (2001), p. 2606.

[10] Y.C. Sui, R. Skomski, K.D. Sorge and D.J. Sellmyer, *Appl Phys Lett* **84** (2004), p. 1525.

[11] Y.C. Sui, R. Skomski, K.D. Sorge and D.J. Sellmyer, *J Appl Phys* **95** (2004), p. 7151.

[12] S.S. Kang, D.E. Nikles and J.W. Harrell, *J Appl Phys* **93** (2003), p. 7178.

[13] S. Sun, C.B. Murray, D. Weller, L. Folks and A. Moser, *Science* **287** (2000), p. 1989.

[14] R. Skomski, *J Phys: Condens Matter* **15** (2003), p. R841.

[15] G.N. Phillips, M. Siekman, L. Abelmann and J.C. Lodder, *Appl Phys Lett* **81** (2002), p. 865.

[16] K.D. Sorge, A. Kashyap, R. Skomski, L. Yue and L. Gao *et al.*, *J Appl Phys* **95** (2004), p. 7414.

[17] L. Gao, L.P. Yue, T. Yokota, R. Skomski and S.H. Liou *et al.*, *IEEE Trans Magn* **40** (2004), p. 2194.

[18] C.T. Rettner, S. Anders, T. Thomson, M. Albrecht and Y. Ikeda *et al.*, *IEEE Trans Magn* **38** (2002), p. 1725.

[19] C.M. Park, J.A. Bain, T.W. Clinton, P.A.A. van der Heijden and T.J. Klemmer, *Appl Phys Lett* **84** (2004), p. 3331.

[20] S.A. Chambers, T. Droubay, D.R. Jennison and T.R. Mattsson, *Science* **297** (2002), p. 827.

[21] R. Skomski, H. Zeng, M. Zheng and D.J. Sellmyer, *Phys Rev B* **62** (2000), p. 3900.

[22] R. Skomski, D. Leslie-Pelecky, R.D. Kirby, A. Kashyap and D.J. Sellmyer, *Scr Mater* **48** (2003), p. 857.